

Lawrence Berkeley National Laboratory

Recent Work

Title

RADIATION INDUCED DEFECTS IN MOLYBDENUM

Permalink

<https://escholarship.org/uc/item/3vq4h6n7>

Author

Rao, Prakash.

Publication Date

1966-09-01

UCRL-17078

University of California

Ernest O. Lawrence
Radiation Laboratory

RADIATION-INDUCED DEFECTS IN MOLYBDENUM

TWO-WEEK LOAN COPY

*This is a Library Circulating Copy
which may be borrowed for two weeks.
For a personal retention copy, call
Tech. Info. Division, Ext. 5545*

Berkeley, California

DISCLAIMER

This document was prepared as an account of work sponsored by the United States Government. While this document is believed to contain correct information, neither the United States Government nor any agency thereof, nor the Regents of the University of California, nor any of their employees, makes any warranty, express or implied, or assumes any legal responsibility for the accuracy, completeness, or usefulness of any information, apparatus, product, or process disclosed, or represents that its use would not infringe privately owned rights. Reference herein to any specific commercial product, process, or service by its trade name, trademark, manufacturer, or otherwise, does not necessarily constitute or imply its endorsement, recommendation, or favoring by the United States Government or any agency thereof, or the Regents of the University of California. The views and opinions of authors expressed herein do not necessarily state or reflect those of the United States Government or any agency thereof or the Regents of the University of California.

Research and Development

UCRL-17078

UNIVERSITY OF CALIFORNIA
Lawrence Radiation Laboratory
Berkeley, California
AEC Contract No. W-7405-eng-48

RADIATION INDUCED DEFECTS IN MOLYBDENUM

Prakash Rao

(Masters Thesis)

September 1966

TABLE OF CONTENTS

ABSTRACT

I. INTRODUCTION 1

II. EXPERIMENTAL PROCEDURE 7

 A. Specimen Preparation for Electron Microscopy 8

 B. Specimen Preparation for Field Ion Microscopy 8

III. EXPERIMENTAL RESULTS 10

 A. General Observations 10

 B. Dependence of Strain-Contrast Images on the
 Diffraction Vector 12

 C. Dependence of Strain Contrast Images on the
 Sign of s 13

 D. Determination of Defect Densities 14

 E. Analysis by Field Ion Microscopy 15

IV. DISCUSSION 17

V. CONCLUSIONS 25

ACKNOWLEDGEMENTS 27

REFERENCES 28

FIGURE CAPTIONS 31

FIGURES 34

RADIATION INDUCED DEFECTS IN MOLYBDENUM

Prakash Rao

Inorganic Materials Research Division, Lawrence Radiation Laboratory,
and Department of Mineral Technology, College of Engineering,
University of California, Berkeley, California

September 1966

ABSTRACT

A combined study, using transmission electron microscopy and field-ion microscopy, of the substructure of neutron irradiated molybdenum has revealed induced damage in the form of small dislocation loops. Bright field electron micrographs give a quantitative estimate of the extent of this damage, and strain contrast imaging in dark field allows the loop plane and Burgers vector to be established. Analysis of these induced defects, using different imaging conditions in dark field, shows that the loops are predominantly of the type $(110) \langle 111 \rangle$ [i.e., loop plane (110) and Burgers vector $\frac{a}{2} \langle 111 \rangle$].

The extension and applicability of the strain contrast theory to radiation induced defects in BCC metals is examined, particularly its usefulness in predicting the interstitial or vacancy character of the defects. Contradictions arise when low-order reflections are used, but the results are less ambiguous for high order reflections and edge on defects. The evidence presented indicates that the defect structure is primarily interstitial.

The irradiation behavior of molybdenum is discussed in terms of present observations. Interstitial impurity atoms play an important role in determining the nature of defects present in the as-irradiated and irradiated-annealed states.

I. INTRODUCTION

Transmission electron microscopy and field-ion microscopy lend themselves admirably to the investigation of radiation induced defects in metals. Point defects of vacancy or interstitial character, which have formed large enough aggregates, are readily observable by transmission electron microscopy, with the result that the thin foil technique has been widely used for defect characterization. The limit of resolution of small defects by diffraction contrast using the thin foil technique is about 20-50Å, depending on, amongst other factors, the thickness of the foil. The remarkable resolution (2-3Å) of the field ion microscope enables the atomic structure of the metal surface to be revealed, and is therefore a more sensitive technique for the detection of radiation damage on a small scale.

Previous work using transmission electron microscopy on neutron irradiated metals has shown that in most cases clustering of point defects occurs to produce prismatic dislocation loops. Neutron damage in metals such as copper,¹ aluminum² and platinum³ results in the formation of a large number of very small loops about 100-150Å in diameter. In many cases positive identification of small defects for which the term "black spots" has been used, was not carried out. Furthermore, since the defects are often very small, it was impossible to determine by direct methods whether they were formed by the condensation of vacancies or interstitials. Fission fragment and heavy ion damage gave rise to large dislocation loops of up to 1500Å in aluminum⁴ and iron.⁵ These were shown to be interstitial in character. Similarly, alpha particle irradiation of metals, such as copper⁶ led investigators to believe that the resulting "black spot" defects were due to vacancy

clusters while the large loops observed were formed from interstitial atoms. However, no definite conclusion as to the nature of radiation induced defects were then obtained. These results were obtained by observing the behaviour of dislocation contrast under varying diffraction conditions, and on the basis of the differences in the rates of diffusion of vacancies and interstitials.

The temperature of irradiation has a marked effect on the nature of the defect structure observed. In copper⁷ and nickel⁸ irradiated at different temperatures resolvable loops were obtained at sufficiently high temperatures of irradiation, while at lower irradiation temperatures "black spot" defects were observed.

Recent work on neutron damage in BCC metals, particularly molybdenum, has yielded interesting results. Downey and Eyre⁹ observed point defect clusters in molybdenum irradiated at reactor ambient temperatures. The defects were deduced to be interstitial in character. Little change was observed in the observable damage on annealing up to 800°C, while the microhardness showed a peak at 170°C followed by steady recovery. Above 800°C, the loops were observed to grow rapidly and finally joined up to form dislocation networks, accompanied by an increase in the rate of recovery of microhardness. Meakin and Greenfield¹⁰ produced a low density of analyzable loops directly during irradiation by subjecting molybdenum to neutron irradiation at a sufficiently high temperature (600°C). Mastel and Brimhall¹¹ suggested that carbon in molybdenum, neutron irradiated at 40°C, promotes the heterogeneous nucleation of clusters and is responsible for the formation of resolvable dislocation loops. In all the work reported to date, the defects have been deduced to be interstitial in nature, with Burgers vector $a/2 \langle 111 \rangle$ and loop plane $\{110\}$. A few dislocation loops with Burgers vector $a \langle 100 \rangle$ have also been

observed at low annealing temperatures.⁹

On the basis of the observations outlined above, Eyre and Bullough¹² predicted the formation of prismatic loops in irradiated BCC metals, with $\{110\}$ loop planes and $\vec{b} = a/2\langle 111 \rangle$ or $\vec{b} = a\langle 100 \rangle$. Taking elastic energy considerations into account, Eyre and Bullough concluded that both the $a/2\langle 111 \rangle$ and $a\langle 100 \rangle$ loops lie on $\{110\}$ and are initially rectilinear but should grow into circular loops and rotate into the pure edge orientation, similarly to the behaviour of perfect loops in FCC metals. Analysis of these prismatic dislocation loops should be possible by double-arc diffraction contrast using the method suggested by Bell and Thomas.^{13a, b}

It may be noted at this stage that only diffraction contrast has been relied upon in the analysis of the resolvable defects in BCC metals. In diffraction contrast the atomic displacements around the defect modify the deviation parameter s , which introduces a phase change in both transmitted and diffracted waves, giving rise to contrast above or below background. The relative position of the dislocation image depends on \vec{g} , the reciprocal lattice vector of the operating reflection, \vec{b} the Burgers vector of the defect, and on the sign of the deviation parameter s , through the product $(\vec{g} \cdot \vec{b})s$. The sign of this product determines the position of the dislocation image.^{13, 14}

However, for dislocation loops smaller than about 200\AA , the images of their sides are not clearly resolvable (as in the case of "black spot" defects observed in the bright field images of irradiated foils). Diffraction contrast as defined above, then becomes unsuitable for analyzing small defects and therefore strain contrast imaging must be used in identifying dislocation loops, as in the case of irradiated or quenched copper.^{15, 16}

Strain contrast images from defects appear as black-white regions divided by a line of no contrast when the crystal is oriented close to the ideal Bragg condition ($s \approx 0$).¹⁷ Strain contrast imaging can detect very small localized strain fields which may not give rise to any diffraction contrast, particularly in dark field. Dark field images obtained by gun-tilting show maximum resolution and contrast.¹⁵ Gun-tilting reverses the direction of \bar{g} compared to bright field, while maintaining the original orientation of the specimen.

The analysis of the loop plane and Burgers vector of strain contrast images from prismatic loops in FCC and BCC metals have been considered elsewhere.^{13,15,18} The validity of the strain contrast theory and its applicability to the determination of defect character have been considered in great detail by Bell et al.^{13,19} It has been shown that the foil thickness, the extinction distance, the deviation parameter, the anomalous absorption parameter, the defect size, defect shape, defect position in the foil, inclination of the defect with respect to the incident beam, defect density and the operating reflection are the parameters which have to be considered for both the bright and dark field cases.¹⁹ In order to determine the character of defects it is essential to know the exact position in the foil, since the analysis of Ashby-Brown¹⁷ is only applicable to defects within $t_0/2$ of the surfaces.

The two important advantages of the field-ion microscope, which have led to its increasing use for the study of radiation damage are: firstly, its resolution of $2-3\text{\AA}$ enables individual atoms to be distinguished and secondly, that field evaporation makes it possible to strip individual atoms or whole atomic layers from the surface under observation in a controlled manner to obtain a three-dimensional picture of the damage.

Previous work on damage introduced by alpha particles,^{20,21} helium ions,²² fission fragments,²³ and neutrons²⁴ has led to the formulation of the nature of radiation induced defects of a few atomic dimensions.

Single vacancies, divacancies and vacancy clusters have been most easily and unambiguously identified as missing atoms, although those inside the unresolved close-packed planes escape observation.²⁵ In order to be sure that the missing atom has not just been removed by field evaporation, only unoccupied sites in the interior of a fully resolved plane, or in the inner part of a homogeneous atom chain should be identified as vacancies. Interstitials have been identified as bright dots appearing at the surface showing up as a result of lattice relaxation.²⁶ The exact mechanism of image formation for these bright spots is not yet clear. Bright spots of a few atom diameters have been observed to alternate with regions of relative perfection in neutron irradiated platinum. Impurities present would be expected to appear in a distinct way due to electronic and geometric mismatch at the surface.²⁵ Impurity atoms would stand out with higher brightness and fuzziness and could be confused with interstitials created by radiation damage.

In all the reported work to date, wire specimens have either been subjected to particle irradiation outside the field ion microscope or in situ. In the present work the microscope has been used for the first time to observe damage produced in bulk specimens subjected to neutron irradiation.

In view of the present state of the theory of strain contrast, this investigation is partly devoted to its extension and applicability to the prediction of the nature of radiation induced defects in BCC metals. The neutron dosage level and temperature of irradiation have been so chosen to

give defect clusters small enough to be analyzed by strain contrast. Two specific cases have been selected. Irradiated molybdenum samples in the as-irradiated and irradiated-annealed conditions have been examined.

A correlation between results obtained from transmission electron microscopy and field ion microscopy has been attempted in this investigation. It will be shown that such a combined study can yield useful results.

II. EXPERIMENTAL PROCEDURE

Specimens used in this investigation were obtained from arc vacuum cast recrystallized molybdenum sheet* in the form of 20 mil/strip. The analysis of the as-received molybdenum sheet is given in Table 1.**

Table 1

Element	Fe	Si	Al	Ca	Cu	W	Sn	B	Ti	Zr	Ni	Cr	Mn
Parts per Million	21	20	5	4	2	100	10	10	1	1	1	1	1

The post-test analysis is compared with the as-received analysis in Table 2.**

Table 2

Element	As-Received (ppm)	Post-Test (ppm)
O ₂	25	13
H ₂	2	1
N ₂	5	2
C	150	160

Prior to irradiation the specimens were annealed in argon for one hour at 1200°C. Specimens were irradiated in an aluminum can stacked (by twos) between aluminum filler pieces, for heat removal, in a helium atmosphere. The irradiations were conducted in the Oak Ridge (ORN-23) reactor at a dosage level of $\sim 1 \times 10^{19}$ nvt, $E_n \geq 1$ Mev at reactor ambient temperature.***

* Supplied by Universal Cyclops Steel Corporation.

** Chemical analysis supplied by Nuclear Materials and Propulsion Operation, General Electric Company, Cincinnati, Ohio.

*** Irradiation supervised by Nuclear Materials and Propulsion Operation, General Electric Company, Cincinnati, Ohio.

A new method for obtaining specimens for both electron and field ion microscopy from the same strip molybdenum was attempted, involving the thin foil technique for electron microscopy and preparation of sharp tips for field ion microscopy from bulk metal rather than from wires.

A. Specimen Preparation for Electron Microscopy

Electron transparent foils were obtained by electropolishing the 20 mil thick molybdenum strip by the window method in an electrolyte of 87.5% methyl alcohol and 12.5% sulfuric acid at 0°C using a D.C. voltage of 6-8 volts. In order to eliminate the possibility of interpreting polishing defects or dirt on the surface as defect clusters caused by irradiation, both the unirradiated control specimen and the as-irradiated specimen were electropolished together under identical conditions. The irradiated foils obtained had negligible ($\beta + \gamma$) activity.

A Siemens Elmiskop I microscope equipped with a double tilting stage was used in this investigation. A two-beam orientation is necessary for contrast analysis of defects. This can be obtained using the double tilting stage. Before attempting any analysis of the bright and dark field micrographs, the diffraction pattern must be oriented properly (180° plus magnetic rotation) with respect to the image.

B. Specimen Preparation for Field Ion Microscopy

A new technique was used for preparing specimens for field-ion microscopy from the bulk metal. The advantage of this method would be the elimination of any discrepancies that might arise in carrying out a study of radiation damage using two different physical forms of the metal, namely strip and wire, thereby eliminating the differences in chemical composition between wire and strip entering the analysis of results. Conventional field-ion specimens are in the wire form.

Masked edges left over after electropolishing the 20 mil strip by the window method, were used as the starting point for the field-ion specimens. The irregular wire-like pieces were electropolished using the thin layer electropolishing technique. The method involves dipping the specimen through a thin layer (5mm) of an aqueous solution of potassium cyanide (10%), floating on top of an inert liquid, carbon tetrachloride. An A.C. supply of 1-40 volts is used, with gas evolution always occurring during specimen preparation.

Great care was exercised in polishing in order to obtain as symmetrical a tip as possible. The specimens were made to revolve about their own axis whilst electropolishing in order to smooth out irregularities. Tip formation resulted easily and the field-ion images were comparable to those obtained from wire specimens.

The field-ion microscope²⁷ used in this investigation is shown in Fig. 6a. The specimen has a sharp tip at the lower end (radius of 100\AA). The microscope chamber is evacuated to a pressure of 1×10^{-7} Torr and the specimen is cooled with liquid nitrogen. Helium is used as the imaging gas and is admitted to the microscope at a pressure of a few microns. On application of a high positive potential to the specimen, the helium gas is ionized at the high field regions existing over protruding atoms on the surface of the specimen, and the helium ions form an image on a fluorescent screen placed a few inches from the specimen. The image obtained approximately represents a stereographic projection of the tip. Surface layers can be removed by field evaporation, whereby under higher applied fields the metal atoms are themselves ionized.

III. EXPERIMENTAL RESULTS

A. General Observations

Initial examination of the molybdenum foil showed that most of the grains had a preferred orientation at and near $\{111\}$ or $\{011\}$. Using the double tilting stage, $\{112\}$, $\{123\}$, $\{135\}$ and $\{012\}$ foil orientations could be obtained. This proved to be useful in that a large proportion of edge-on loops were obtained which facilitates the applicability of the strain contrast theory in dark field (i.e., $\vec{g} \cdot \vec{R}$ is maximum for contrast, where \vec{R} is the displacement vector associated with the loop).

Bright field micrographs of unirradiated molybdenum (Fig. 1a) were free of defects observed in irradiated molybdenum. The bright field micrographs of as-irradiated (1×10^{19} nvt; $E_n \geq 1\text{MeV}$) molybdenum show a very large number of spot defects (Fig. 1b). Figure 1c shows the dark field micrograph of the same area as in Fig. 1b. The very large number of black-white lobed images makes analysis impossible. The high density of induced defects results in overlapping strain fields, and a number of reversals in contrast are evident on both sides of the extinction contours in the bright and dark field images. It can be assumed that these strain contrast images arise from radiation induced defects and not as a result of electropolishing,²⁸ since the unirradiated foil electropolished simultaneously did not show these defects. In addition, the number of observable defects increases towards the thicker regions of the foil, as would be expected of an evenly distributed damage structure. A count of the number of images observable in Fig. 1b shows that the defect density increases from $\sim 4 \times 10^{16}$ defects per cm^3 at a foil thickness of $2t_0$, to $\sim 6.42 \times 10^{16}$ defects per cm^3 at thickness of $4t_0$. The strain contrast images are in best contrast at foil thicknesses of an odd number of extinction distances.¹⁹

Bright field micrographs show denuded regions of defects to $\sim 400\text{\AA}$ on each side of grain boundaries (Fig. 2a). Some micrographs show preferential damage formation.

Figure 2d shows a dark field micrograph of a line of defects in the $\langle 111 \rangle$ direction with parallel lines of no contrast (marked X-X). The bright field micrograph (Fig. 2c) of the same area shows black spot defects evenly distributed, and no preferential damage is observable in the X-X direction. All the strain contrast images have the same line of no contrast and streaking direction. The line of no contrast separates the black and white portions of the strain contrast image, while the streaking direction represents the major axis of the black-white image.

Although under the conditions of irradiation there should be very little direct contact type fission fragment damage, it is possible that (a) the aluminum in contact with the molybdenum would, by sputtering, enter the molybdenum specimen to cause a different type of track, or (b) perhaps any trace quantities of boron may, through the thermal neutron (n, α) reaction, release the helium and lithium atoms to cause a different type of damage structure. The similarity to a low angle boundary is evident, but the large distance of separation between the dislocation lines (1000\AA) and the unchanged selected area diffraction pattern seems to indicate preferential damage formation. Region A in Fig. 2e resembles a displacement spike, with continuous tracks caused by primary and secondary knock-ons. The nature of the tracks indicates fission fragment type damage.

Experiments with irradiated molybdenum [1×10^{19} nvt; $E_n \geq 1\text{MeV}$] annealed at 760°C for one hour yielded more interesting results. Three sets of experiments were performed. Firstly, the same area was observed in bright

and dark field using different diffraction vectors, keeping s constant. Secondly, another area was observed in bright and dark field changing the sign of s while keeping the diffraction vector constant. Thirdly, an area was observed in dark field at $s < 0$ with different operative diffraction vectors.

B. Dependence of Strain-Contrast Images on the Diffraction Vector

The same specimen area can be imaged with different operating diffraction vectors, resulting in different extinction distances. Those dislocation loops which do not change sign for a sufficient variation of the extinction distance lie immediately below one of the surfaces. Then the dark-field image would give the correct nature of the loops.²⁸ That is, the number of "wrong sense" images decreases as the order of reflection increases.

Figure 3 shows bright and dark field micrographs of the same area at $s > 0$. Figures 3a and 3b have the same $\langle 110 \rangle$ diffraction vector operating in bright and dark field, while Figure 3c has a $\langle 112 \rangle$ diffraction vector operating on the same area in dark field.

The foil orientation, using both the $\langle 110 \rangle$ and $\langle 112 \rangle$ beams, was accurately determined using the BCC Kikuchi map developed by Okamoto et al.²⁹ Stereograms suitably oriented give projections of the $\langle 111 \rangle$, $\langle 110 \rangle$ and $\langle 011 \rangle$ directions which are of importance in BCC metals. As shown in Fig. 3, the lines of no contrast are distinctly normal to the projected $\langle 111 \rangle$ directions indicating that the Burgers vectors of these defects are of the type $\frac{a}{2}\langle 111 \rangle$.¹³ The direction of black-white streaking is in the projected $\langle 110 \rangle$ directions indicating that the loop planes of these planar defects are $\{110\}$.

Examination of Figs. 3b and 3c show that all the black-white images (A, B, C, D, and E) visible have the same (parallel) lines of no contrast and direction of streaking, and are, therefore, of the same type - same Burgers vector and loop plane. Since in (b) and (c) the lines of no contrast and the direction of black-white streaking do not change with the two different diffraction vectors, it is evident that the Burgers vector and loop plane of these defects are independent of the operating diffraction vector, and therefore must be plate shaped defects, i.e., loops.

C. Dependence of Strain Contrast Images on the Sign of s

The sign of the deviation parameter s determines which part of the foil is in good contrast. In dark field, when $s < 0$, the top of the foil is in good contrast while when $s > 0$ the bottom of the foil is in good contrast.¹⁹ Using these two imaging conditions, the position of the defect in the foil can be approximately estimated. However, when $s \neq 0$ the effective extinction distance is decreased.

Figures 4 and 5 show areas of irradiated - annealed molybdenum observed in bright and dark field with the same operating $\langle 112 \rangle$ beam under conditions of s negative and s positive. The approximate position of each of the marked defects, determined on the basis of visibility under different signs of s , are tabulated alongside each of the figures. An analysis of the Burgers vector and loop plane of each defect is also given.

Some of the larger defects show faint double-arc contrast in bright field. Loops unsuitably oriented to give good strain contrast images lie in the plane of the foil and will give good double arc contrast. Defect X in Fig. 4, for example, shows double arc contrast with a clear line of no contrast parallel to the $[10\bar{1}]$ projected direction with the $[1\bar{1}1]$ pro-

jected direction normal to the line of no contrast. The displacement of the double-arc image is in the $[0\bar{1}0]$ projected direction. According to the double-arc model, the loop plane of this particular loop is $[\bar{1}0\bar{1}]$ and Burgers vector $\frac{a}{2}\langle 1\bar{1}1 \rangle$. For the analysis of these radiation induced defects in Figs. 4 and 5, the foil orientation was accurately determined using the BCC Kikuchi map.²⁹

D. Determination of Defect Densities

An estimation of the density of defect clusters was attempted using bright field electron micrographs enlarged to a magnification of 204,000x. A count of the number of defects per unit volume in both the as-irradiated and irradiated-annealed states was made near the edge of the foil where extinction contours allow the foil thickness to be estimated. The results are shown in Table 3.

TABLE 3

Irradiation Condition	Number of Defects per cm ³	Average Defect Diameter (Å)	Theoretical number of Displacements/cm ³
As-irradiated	5.04×10^{16}	100	2.92×10^{21}
Irradiated-annealed at 760° (1 hour)	1.44×10^{16}	200	

The high density of defects in the as-irradiated foils makes it difficult to distinguish between superimposed clusters. The number of clusters/cm³ can be compared to the theoretical number of displacements per unit volume, (N_{Dt}) . Using the Kinchin and Pease model,³⁰

$$N_{Dt} = \frac{L_c (2 - L_c / E_{max})}{4E_f}$$

where L_c = threshold energy for production of knock-ons.

E_{max} = maximum energy transferred to atoms by neutrons

E_f = minimum energy for focusing,

and the values of each of these variables suggested for molybdenum by Downey and Eyre,⁹ the theoretical number of displacements/cm³ under the present irradiation conditions is shown in Table 3.

E. Analysis by Field Ion Microscopy

Micrographs of pure molybdenum tips, prepared from wire specimens, taken at liquid nitrogen temperature, show adequate resolution (Fig. 6b). The individual atoms on the (111) planes are not fully resolvable as the field applied to cause field evaporation results in stressing the (111) area. The (011) and (112) planes are clearly resolved.

Micrographs of irradiated molybdenum tips prepared from bulk give slightly distorted images which may be due to poor electropolishing (resulting in asymmetrical tip formation). In one particular sequence, streaking was observed, as shown by the single streak along the (110) planes in Fig. 7a. On field evaporation, the streak disappeared leaving behind an incomplete inner ring of (110) atoms. On further field evaporation, complete (110) rings were obtained (Fig. 7b). Streak contrast from field-ion micrographs has been discussed elsewhere.^{31,32,33} Considerable streaking has been observed in cold-worked neutron irradiated tungsten³¹ and is associated with the interaction of point and line defects. The precise role of electropolishing and clustering of interstitial impurities in streak contrast is not known.^{31,32,33}

Other observations on irradiated molybdenum field-ion micrographs included the appearance of bright spots (Fig. 7c). The size of these bright spots (a few atom diameters) as well as their enhanced local intensity indicate a local disturbance of the normal arrangement of the material. These may be due to either interstitial atoms bulging out of the surface or due to impurities in the material (see Table 1).

Inspection of some 100 field evaporated $\{110\}$ planes failed to reveal vacancies. The density of vacancies must be very low. With the limited experimental material available, it is not possible to explain the lack of vacancies.

IV. DISCUSSION

The discussion is divided into two sections, the first dealing with the extension of the strain contrast theory to radiation induced defects in BCC metals, the second dealing with the irradiation behavior of molybdenum.

1. Extension of the Strain Contrast Theory to Radiation Induced Defects in BCC Metals

An interesting observation that can be made from Figs. 3, 4, and 5 is that every one of the analysed strain contrast images have the black side of the black-white image in the direction of the operating diffraction vector in dark field (it can be seen that about 70% of all clearly visible defects have been analysed). On the basis of theory this would mean that most of the strain contrast images are from interstitial loops. Bell et al.¹⁹ have pointed out, however, that in FCC systems (primarily aluminum and its alloys) it does not seem possible to unambiguously determine vacancy and interstitial strain fields using strain contrast imaging except for the special case of defects within $t_0/2$ of any surface. The various parameters that have to be considered for both bright and dark field cases have been listed.¹⁹ Figures 8a and 8b show cases where reversals of images were observed in irradiated-annealed molybdenum foils at $s < 0$. Even in these cases, the number of "vacancy" type images seem to be few in number.

Amongst other observations, it is found that the best strain contrast image is observed in foils for which the thickness is an odd number of extinction distances.¹⁹ The length of the black and white lobes of the strain contrast image vary with the particular sign of s and position in the foil. In dark field, the white part is equal in length to the dark

part (measured along the direction of streaking at $s = 0$. When $s < 0$, the white part is longer than the black part, while when $s > 0$, the opposite is true, because of the change in background.

Since dark field micrographs exhibit best contrast around defects near the lower surface of the foil for $s > 0$ and near the upper surface of the foil for $s < 0$, by imaging under these conditions (Figs. 4 and 5), it is shown that the induced defects are evenly distributed in the foil. However, defects near the center of the foil will show up under both imaging conditions, especially when the foil is thin and the loops are edge on. However, with higher order reflections, the larger extinction distances are more sensitive to changes in s , making imaging conditions critical. The size of the defect in relation to t_0 and the foil thickness is, therefore, of considerable importance, especially in the case of planar defects.

If the specimen is oriented such that the Burgers vector and the normal to the habit plane are in the plane of the foil, then definite statements concerning the nature of the defects can be made.¹⁹ Table 4 shows the angles between the foil normal and the direction of the Burgers vector, and the normal to the loop plane calculated for three cases. It can be seen that since the Burgers vector and the normal to the loop plane nearly always lie in the plane of the foil, the conclusions as to defect character should be correct.

Defect density is another factor which can affect the character of strain contrast images. No attempt was made at analysing the defect structure in as-irradiated molybdenum because of the proximity of other defects.

TABLE 4

Foil Orientation	$\langle 112 \rangle$	$\langle 123 \rangle$	$\langle 123 \rangle$
Direction of Burgers Vector	$\bar{1}\bar{1}\bar{1}$	$11\bar{1}$	$11\bar{1}$
Direction of Loop Plane Normal	$\bar{1}10$	$01\bar{1}$	$0\bar{1}\bar{1}$
Angle Between Foil Normal and Burgers Vector	62°	90°	90°
Angle Between Foil Normal and Loop Plane Normal	90°	79.2°	71°

It has been shown theoretically that the image to be expected from a small defect depends critically upon its position or distance from the foil surface as measured in extinction distances of the operating reflection.²⁸ This image can either be white on the side of the operating reflection (in dark field) or black on the side of the operating reflection if the defect is half an extinction distance above or below these positions. Using reflections with a longer extinction distance is the recommended solution for causing defects, which may give complications in characterisation, to form an image from which the nature of the defect can be unambiguously determined.

For this purpose, the same area of an irradiated-annealed foil of molybdenum was examined using the $\langle 112 \rangle$, $\langle 310 \rangle$ and $\langle 222 \rangle$ operating reflections in dark field at $s < 0$ such that only those defects near the top of the foil were in good contrast in each case. At $s > 0$, there were very few reversals in image sense.

An increase in the number of strain contrast images was registered with increasing orders of reflection. This would be expected from an increase in the extinction distance, for nearly constant s . A count was made of the number of observable images ($> 100\text{\AA}$) with increasing $\langle 112 \rangle$, $\langle 310 \rangle$ and $\langle 222 \rangle$ reflections (Fig. 9a,b,c), and of the number of "interstitial" and "vacancy" images. The results are summarized in Table 5.

It is observed that the number of "vacancy" images decreases with increasing diffraction vector. Similar counts in ion irradiated copper show a decrease in the number of "interstitial" images with increasing diffraction vector.^{16b}

There is a marked decrease in the number of so-called vacancy defects when the $\langle 222 \rangle$ reflection is used, but the resolution in dark-field decreases rapidly as the order of reflection increases making the count of the number of "wrong sense" images very approximate. It is observed that the intensity and extent of contrast of the images are reduced with increasing diffraction vector. Since the size of the observed strain contrast images depends on the extent of contrast, the image size decreases with increasing diffraction vector. However, the "wrong-sense" images, which are larger in width for lower order reflections, tend to be of the same size as the "right-sense" images for higher order reflections.

Though, in general, strain contrast imaging techniques do not seem to be applicable to the problem of distinguishing between vacancy and interstitial type defects, in this particular case, the evidence presented indicates that the induced defects in neutron irradiated molybdenum are predominantly interstitial in character. It must be noted, however, that the number of parameters that can affect the characterisation of these defects are so many¹⁹ that a definite conclusion at this stage seems unlikely.

TABLE 5

Operating Reflection (hkl)	112	310	222
Extinction Distance (Å)	342	472.5	529
Number of Strain Contrast Images	147	286	338
Number of Interstitial Images*	111	229	303
Number of Vacancy Images*	36	57	35
Ratio of Interstitial: Vacancy	12:3	10:2	10:1

* As predicted by strain contrast theory.

2. Irradiation Behavior of Molybdenum

Theory predicts that as primary knock-ons are slowed down, they displace practically every atom that they encounter, creating highly localised regions of damage known as displacement spikes.³⁴ Regions of dispersed single defects would also be expected in the early stages of the collision sequence since the displacements are widely separated. The spike region itself consists of a central core of vacancies surrounded by interstitial atoms. This arrangement is inherently unstable and will be even more so at elevated temperatures. Interstitial-vacancy recombination has been shown to occur at temperatures as low as 20°K as a result of electrical resistivity studies on electron irradiated molybdenum.³⁵ Irradiation at reactor ambient temperature would, therefore, cause considerable self-annealing within the spikes resulting in vacancy-interstitial annihilation. A certain proportion of the interstitials are conveyed away from the spike region by diffusion or by focusing leaving behind a cluster of vacancies. Such vacancy clusters would survive self-annealing, and have been directly observed in a field-ion microscope study of neutron irradiated tungsten.³¹

Vacancies in molybdenum have been found to be immobile to 150-200°C.³⁶ Surviving vacancies can, therefore, be expected to remain as dispersed clusters, while single vacancies from earlier collision sequences will be randomly distributed.

Previous workers on neutron damage in molybdenum have advanced several reasons for the lack of observed vacancies in irradiated molybdenum.^{9,10,11} Meakin and Greenfield¹⁰ have shown that impurity-vacancy interactions are probably responsible for the trapping of vacancies. The mobility of the particular defect created by the primary event would decide the future course. Relatively immobile vacancy clusters would grow on annealing to form large defect clusters. Examples marked B in Fig. 8 show perfect vacancy strain contrast in dark field and are larger (size measured along the line of no contrast) than those which show interstitial strain contrast. Interstitials moving away from the spike region are relatively mobile and can contribute to the growth of dislocation loops.

The impurity content has an important role to play in determining the annealing behaviour of irradiated molybdenum. The most likely traps are interstitial impurity atoms. The total interstitial impurity content of the molybdenum (carbon and nitrogen) is 1.03×10^{19} atoms/cm³ (from Table 2). Interstitials created by radiation damage would be attracted by interstitial impurity atoms finally resulting in the development of clusters as more and more interstitials migrate to the trapping centers. Downey and Eyre⁹ concluded that the interstitial cluster sizes will depend on the density and distribution of impurity traps.

Annealing characteristics, as indicated by recovery in electrical resistivity and lattice parameter, show a major recovery peak at

150-200°C.³⁶ This has been attributed to the diffusion of vacancies to interstitial impurities.³⁶ Since this process does not account for the recovery in lattice parameter, an alternative suggestion⁹ is the mutual annihilation of single vacancies and interstitials, following second order kinetics.³⁷ The recovery of microhardness in the 150-200°C region is also associated with the migration of vacancies to form compact clusters.⁹

Comparing the damage structure of as-irradiated molybdenum with that in irradiated molybdenum annealed at 760°C for 1 hour, the annealing seems to have had little effect on the number of observable defects (Table 3). These results agree with those of Downey and Eyre⁹ who attributed the relatively unchanged 500-800°C annealing stage to the break-up of vacancy clusters and the subsequent recombination and mutual annihilation with interstitial clusters in high purity molybdenum.

It is interesting to note that no vacancies were detectable in the field ion microscopy of irradiated molybdenum, though bright spots were observed, which could indicate predominantly interstitial damage. It is not possible at this stage, however, to distinguish between interstitial defects created by radiation damage and interstitial impurity atoms. The high density of interstitial impurity atoms (1.03×10^{19}) prevents definite characterisation.

Two types of loops have been observed in BCC metals, with Burgers vectors $\frac{a}{2}\langle 111 \rangle$ and $a\langle 100 \rangle$. Observations on the irradiated molybdenum annealed at 760°C for 1 hour indicate the predominantly $\frac{a}{2}\langle 111 \rangle$ loops are present. Interstitial loops in BCC metals can nucleate on the $\{110\}$ plane with Burgers vector $\vec{b} = \frac{a}{2}\langle 110 \rangle$, enclosing a stacking fault. They can shear in the early stage of growth, in either a $\langle 100 \rangle$ or a $\langle 110 \rangle$ direction to remove the stacking fault and produce loops with $\vec{b} = \frac{a}{2}\langle 111 \rangle$.

or $\bar{b} = a\langle 100 \rangle$, respectively.¹² This suggests that a $\langle 110 \rangle$ shear occurs even at higher temperatures resulting in a large proportion of loops with $\bar{b} = \frac{a}{2}\langle 111 \rangle$. Since on annealing to 760°C, there is a predominance of $\frac{a}{2}\langle 111 \rangle$ loops, it can be assumed that the higher energy $\langle 110 \rangle$ shear requires thermal energy to assist it, and would, therefore, occur only at elevated temperatures, as suggested by Eyre and Bullough.¹² All the loops observed by double arc contrast are circular in shape, in keeping with the observation that $\frac{a}{2}\langle 111 \rangle$ type loops have predicted to be circular while $a\langle 100 \rangle$ type loops retain square shapes.¹² In the 500-800°C annealing stage $\frac{a}{2}\langle 111 \rangle$ loops predominate, while on annealing to above 1000°C, the higher thermal energy supplied would give rise to $a\langle 100 \rangle$ loops, exclusively.

Loops observed by double-arc contrast obey the basic rules set by Bell and Thomas¹³ for the identification of prismatic loops in BCC systems. The loop plane can be uniquely identified for $\{110\}$ loops though each loop has two possible Burgers vectors of the type $\frac{a}{2}\langle 111 \rangle$. These loops are characterised by a major axis along $[110]$ and a minor axis along $[001]$ which is normal to the major axis.¹³

Characterisation of the loop plane and Burgers vector of strain contrast images of prismatic loops in irradiated molybdenum follow the image characteristics predicted elsewhere,¹³ in that the line of no contrast of $\{110\}$ $\langle 111 \rangle$ loops is normal to the projected $\langle 111 \rangle$ direction, and the image is skewed about the line of no contrast in $\langle 110 \rangle$ (Fig. 10).

V. CONCLUSIONS

Investigation of neutron irradiated molybdenum foils using transmission electron microscopy reveals "black spot" defects in bright field micrographs. It is not possible to determine the nature of these defects by imaging by diffraction contrast. Strain contrast imaging provides a means of detecting induced defects which are too small to give rise to any significant diffraction contrast. Bright field micrographs do, however, show characteristic damage structure, such as denuded regions near grain boundaries and fission fragment type damage.

Strain contrast imaging of small defects allows loop plane and Burgers vector analysis, and, to a certain extent, the characterisation of the nature of induced damage. Such an analysis is possible by varying the imaging conditions in dark field. Using different operating diffraction vectors in dark field, it has been shown that the lines of no contrast and the direction of streaking of the black-white lobed images are independent of the operating diffraction vector. This shows that the defects giving rise to strain contrast images are definitely loops.

By varying the sign of the deviation parameter s , and using the criteria that in dark field the top of the foil is in good contrast when $s < 0$ and the bottom of the foil is in good contrast when $s > 0$, it has been shown that the defects are evenly distributed in the foil. An estimation of the defect densities reveals little change in the relative number of defect clusters on annealing to 760°C .

Extending the double arc model and strain contrast imaging to radiation induced defects in FCC metals, it is observed that there is good agreement with predictions.¹⁸ Definite analysis of the loop plane and Burgers vector is possible using both imaging techniques. In this case it is found that most of the loops are of the type $\{110\} \langle 111 \rangle$.

An interesting observation is that a large proportion of the analysed strain contrast images have the black side of the black-white image in the direction of the operating diffraction vector in dark field, meaning, on the basis of theory, that the strain contrast images arise from interstitial loops. It has been pointed out elsewhere¹⁹ that it does not seem possible to unambiguously determine (in FCC systems) vacancy and interstitial strain fields using strain contrast imaging unless various parameters are considered. Since in most of the observed cases the Burgers vector and the normal to the loop plane were approximately in the plane of the foil, the defect characterisation of those images showing interstitial strain contrast is likely to be correct.

Imaging in dark field using increasing orders of reflection shows an increasing number of strain contrast images, with a decreasing ratio of vacancy to interstitial images, as predicted by the strain contrast theory.

Field ion microscopy reveals streaking and image distortion which could arise from several factors, including radiation damage. Interstitial atoms appear as bright spots, but may be confused with impurities present, which give rise to similar contrast. The definite lack of observed vacancies in field ion micrographs can be coupled with previous observations that the damage substructure in neutron irradiated molybdenum is primarily interstitial.

The evidence presented suggests that the defect structure in neutron irradiated molybdenum annealed at 760°C for 1 hour consists primarily of interstitial loops with a few comparatively large vacancy clusters. The size of these defects varies from about 100Å in the as-irradiated state to about 200Å in the specimens annealed at 760°C.

ACKNOWLEDGEMENTS

The author is deeply grateful to Professor G. Thomas for his guidance, encouragement, unfailing patience and support during this research. Thanks are also due to Dr. J. Moteff of the Nuclear Materials and Propulsion Operation, General Electric Company, Cincinnati, Ohio, for having supplied the material used in this investigation, and to Dr. S. Ranganathan for his guidance and help in field ion microscopy.

This work was done under the auspices of the United States Atomic Energy Commission through the Inorganic Materials Research Division of Lawrence Radiation Laboratory, University of California, Berkeley.

REFERENCES

1. J. Silcox and P. B. Hirsch, *Phil. Mag.* 4, 1356 (1959).
2. T. K. Bierlein and B. Mastel, Fifth International Congress for Electron Microscopy, Philadelphia (Academic Press, New York, 1962) F-5.
3. E. Reudl, P. Delavignette and S. Amelinckx, Symposium on Radiation Damage in Solids and Reactor Materials, Venice (International Atomic Energy Agency, 1962) p. 363.
4. K. H. Westmacott, A. C. Roberts and R. S. Barnes, Fifth International Congress for Electron Microscopy, Philadelphia (Academic Press, New York, 1962) F-11.
5. D. J. Mazey, R. S. Barnes and A. Howie, *Phil. Mag.* 7, 1861 (1962).
6. R. S. Barnes and D. J. Mazey, *Phil. Mag.* 5, 1247 (1960).
7. I. G. Greenfield and H. G. F. Wilsdorf, *Naturwissenschaften* 47, 395 (1963).
8. I. G. Greenfield and H. G. F. Wilsdorf, *J. Phys. Soc. Japan, Supp. III*, 18, 20 (1963).
9. M. E. Downey and B. L. Fyre, *Phil. Mag.* 11, 53 (1965).
10. J. D. Meakin and I. G. Greenfield, *Phil. Mag.* 11, 277 (1965).
11. B. Mastel and J. L. Brimhall, *Acta Met.* 13, 1109 (1965).
12. B. L. Eyre and R. Bullough, *Phil. Mag.* 11, 31 (1965).
13. (a) W. L. Bell and G. Thomas, UCRL-16271, Sept. 1965; (b) W. L. Bell and G. Thomas, *Phil. Mag.* 13, 395 (1966).
14. G. Thomas, Thin Films (ASM) 227 (1964); also UCRL-11009, (Oct. 1963).
15. W. Bell, D. M. Maher and G. Thomas, Lattice Defects in Quenched Metals (Academic Press, New York, 1965) p. 739.
16. (a) R. V. Hesketh and G. K. Rickards, *Proc. Roy. Soc.* A289, 353 (1966); (b) R. V. Hesketh and G. K. Rickards, *Phil. Mag.* 13, 1069 (1966).

17. M. F. Ashby and L. M. Brown, *Phil. Mag.* 8, 1063 (1963).
18. W. L. Bell (M.S. Thesis) University of California, Berkeley, UCRL-16024, June 1965.
19. W. L. Bell, D. M. Maher and G. Thomas, *Proc. Harwell Conference*, UCRL-16955 (July 1966).
20. E. W. Müller, Proc. Fourth International Symposium on Reactivity of Solids, Amsterdam (1960) p. 682.
21. D. G. Brandon, M. J. Southon and M. Wald, Proceedings International Conference on Properties of Reactor Materials and the Effects of Radiation Damage (Butterworths, London, 1961) p. 113.
22. M. K. Sinha and E. W. Müller, *J. Appl. Phys.* 35, 1256 (1964).
23. L. M. Bowkett, L. T. Chadderton, H. Norden and B. Ralph, *Phil. Mag.* 11, 651 (1965).
24. M. J. Attardo and J. M. Galligan, *Phys. Rev. Letters* 14, 641 (1965).
25. E. W. Müller, *J. Phys. Soc. Japan* 18, Suppl. II (1963).
26. E. W. Müller, Advances in Electronics and Electron Physics, VIII (Academic Press, New York, 1960) p. 83.
27. S. Ranganathan, *Current Science* 35, 6 (1966) and UCRL-16520, (Oct. 1965).
28. M. Rühle, M. Wilkens and U. Essmann, *Phys. Stat. Sol.* 11, No. 2, 819 (1965).
29. P. R. Okamoto, E. R. Levine and G. Thomas, UCRL-16897 (June 1966).
30. G. H. Kinchin and R. S. Pease, *Rep. Progr. Phys.* 18, 1 (1955).
31. S. Ranganathan, K. M. Bowkett, J. Hren and B. Ralph, *Phil. Mag.* 12, 841 (1965).
32. D. G. Brandon, *Phil. Mag.* 13, 1085 (1966).
33. B. Ralph and K. M. Bowkett, *Phil. Mag.* 13, 1283 (1966).
34. J. Brinkman, *J. Appl. Phys.* 25, 961 (1954).

35. P. G. Lucasson and R. M. Walker, Phys. Rev. 127, 485 (1962).
36. D. E. Peacock and A. A. Johnson, Phil. Mag. 8, 563 (1963).
37. J. Nihoul, IAEA Symposium on Radiation Damage in Solids, Vol. I, 309 (1962).

FIGURE CAPTIONS

- Fig. 1 (a) Bright field micrograph of unirradiated molybdenum.
(b) Bright field micrograph of as-irradiated (1×10^{19} nvt; $E_n \geq \text{MeV}$) molybdenum showing a very large number of spot defects. A defect density count shows that the number of observable defects increases with foil thickness.
(c) Dark field micrograph of the same irradiated area showing a high density of induced defects.
- Fig. 2 (a) Bright field micrograph showing denuded regions of defects to $\sim 400\text{\AA}$ on each side of a grain boundary.
(b) Bright field image of a different type of damage structure than that expected from neutron damage.
(c) Bright field micrograph showing black spot defects evenly distributed with no preferential damage observable in the X-X direction.
(d) Dark field image of the same area as in (c) showing preferential damage in the $\langle 111 \rangle$ direction as represented by a line of defects (marked X-X).
(e) Bright field micrograph showing a continuous track, with a region A which resembles a displacement spike. The nature of the tracks indicates fission fragment type damage.
- Fig. 3 Bright and dark field micrographs of the same area in neutron irradiated (1×10^{19} nvt; $E_n \geq 1 \text{ MeV}$) molybdenum annealed at 760°C for 1 hour. (a) and (b) have the same $\langle 110 \rangle$ diffraction vector operating in bright and dark field, while (c) has a $\langle 112 \rangle$ diffraction vector operating in dark field. Comparison of the line of no contrast and streaking direction with the important

$\langle 100 \rangle$, $\langle 110 \rangle$ and $\langle 111 \rangle$ projected directions shows that the defects A, B, C, D and E are of the same type - viz $\{110\}$ loop planes and $\langle 111 \rangle$ Burgers vector.

Fig. 4 Bright and dark field images with the same operating $\langle 112 \rangle$ beam. (a) Bright field micrograph, (b) dark field images at $s < 0$ bringing the top of the foil into good contrast; (c) dark field images at $s > 0$ bringing the bottom of the foil into good contrast: The approximate positions of each of the marked defects are tabulated alongside with an analysis of the Burgers vector and loop plane of each defect; (d) double arc contrast shown by a defect, X, is analysed in terms of the line of no contrast being parallel to a projected $\langle 110 \rangle$ direction and normal to a projected $\langle 111 \rangle$ direction.

Fig. 5 Dark field images with the same operating $\langle 112 \rangle$ beam. (a) and (c) are at $s < 0$ while (b) and (d) are at $s > 0$. The approximate positions of each of the marked defects along with their loop plane and Burgers vector analysis are tabulated alongside, as in Fig. 4.

Fig. 6 (a) Schematic diagram of the field-ion microscope operated at liquid nitrogen temperature.

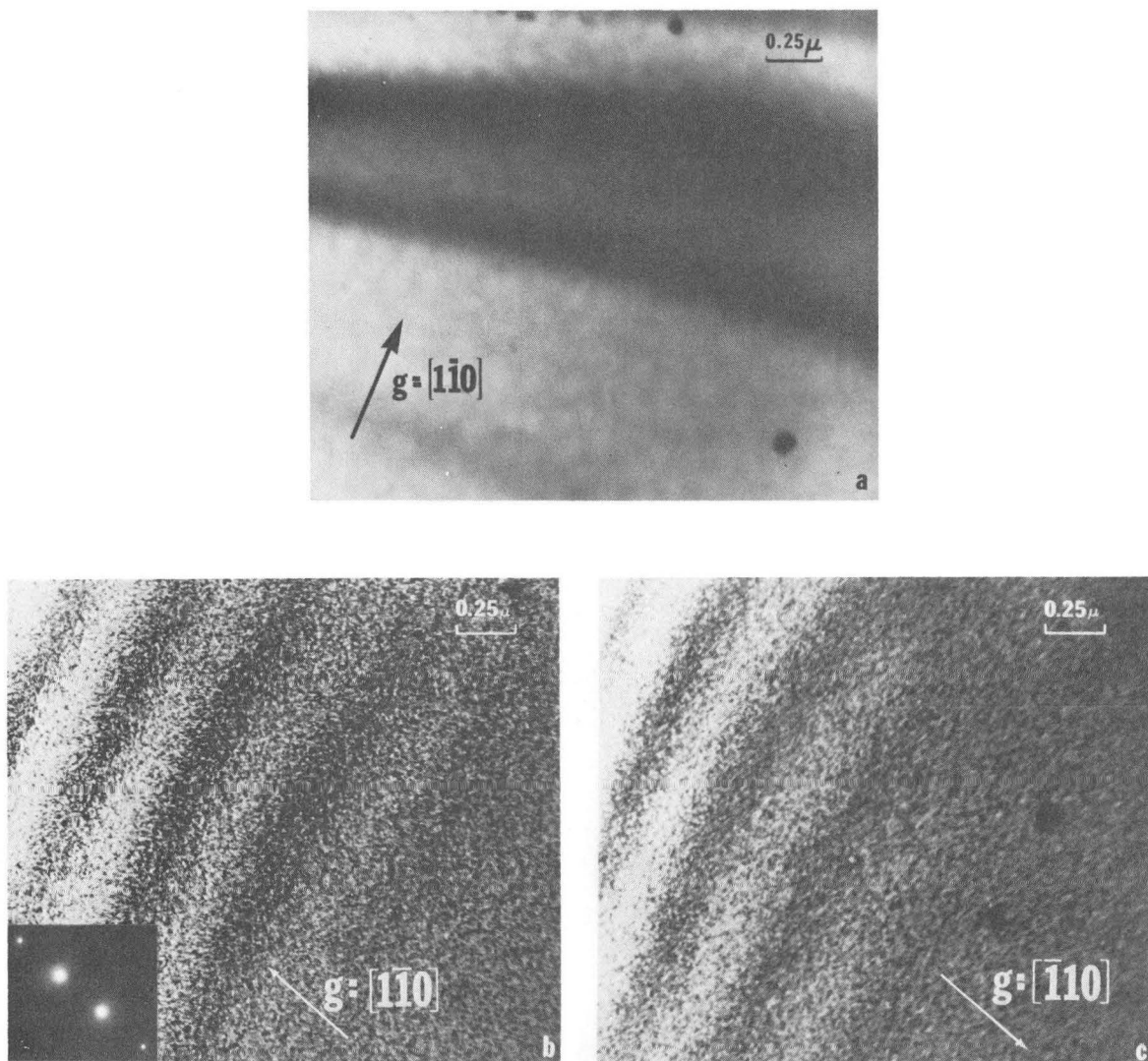
(b) Helium field ion micrograph of pure molybdenum at 77°K .

Fig. 7 Helium field-ion micrographs of irradiated molybdenum tips prepared from bulk specimens. (a) A single streak appears along a $\langle 110 \rangle$ plane, and disappears on field evaporation (b); bright spots (A) of a few atom diameters appear in some of the micrographs indicating a local disturbance of the normal arrangement of atoms (c).

Fig. 8 Dark field micrographs showing image reversals in irradiated-annealed molybdenum foils at $s < 0$. Defects marked A in (a) and (b) show "interstitial" contrast while defects marked B show "vacancy" contrast. Comparison with the important projected directions alongside show that all the defects marked A are of the type $\{110\} \langle 111 \rangle$.

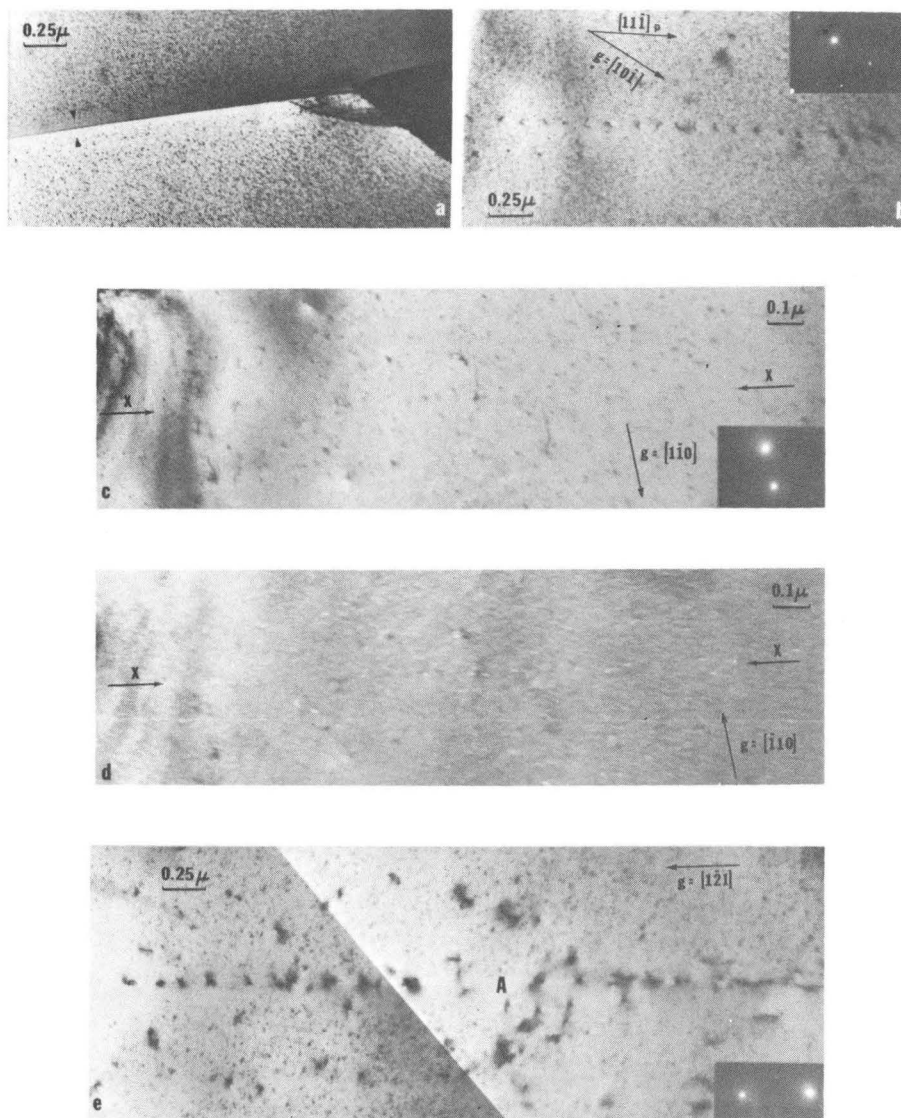
Fig. 9 Dark field images of the same area at $s < 0$ imaged using different diffraction vectors. The increase in the number of observable images with increasing diffraction vector is evident in (a), (b) and (c) (see Table 5).

Fig. 10 Asymmetrical dark field strain contrast images (A) showing clearly the line of no contrast separating the white and black portions of the image. The normal to the line of no contrast gives the direction of the Burgers vector and the direction of streaking gives the loop plane normal direction (see alongside).



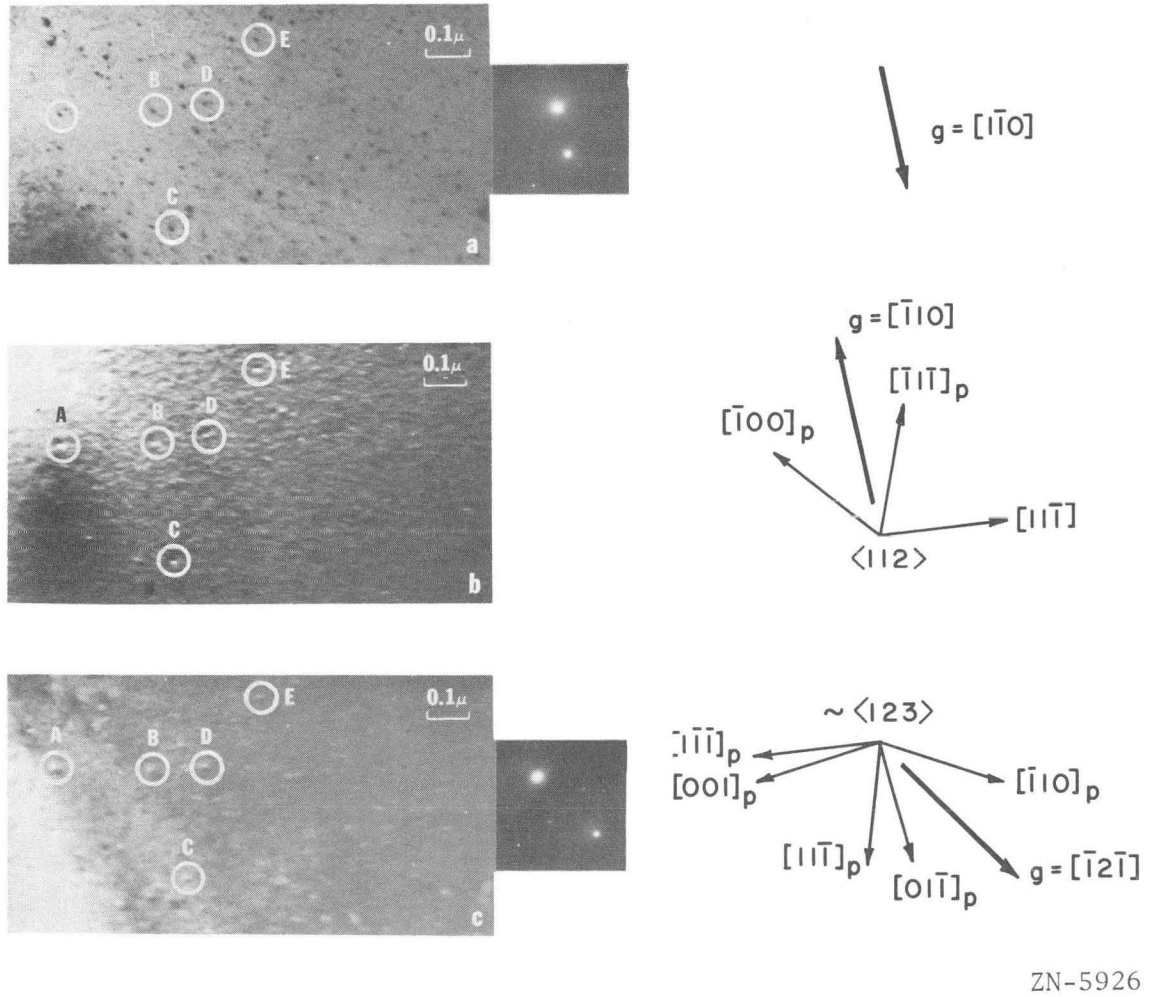
ZN-5929

Fig. 1



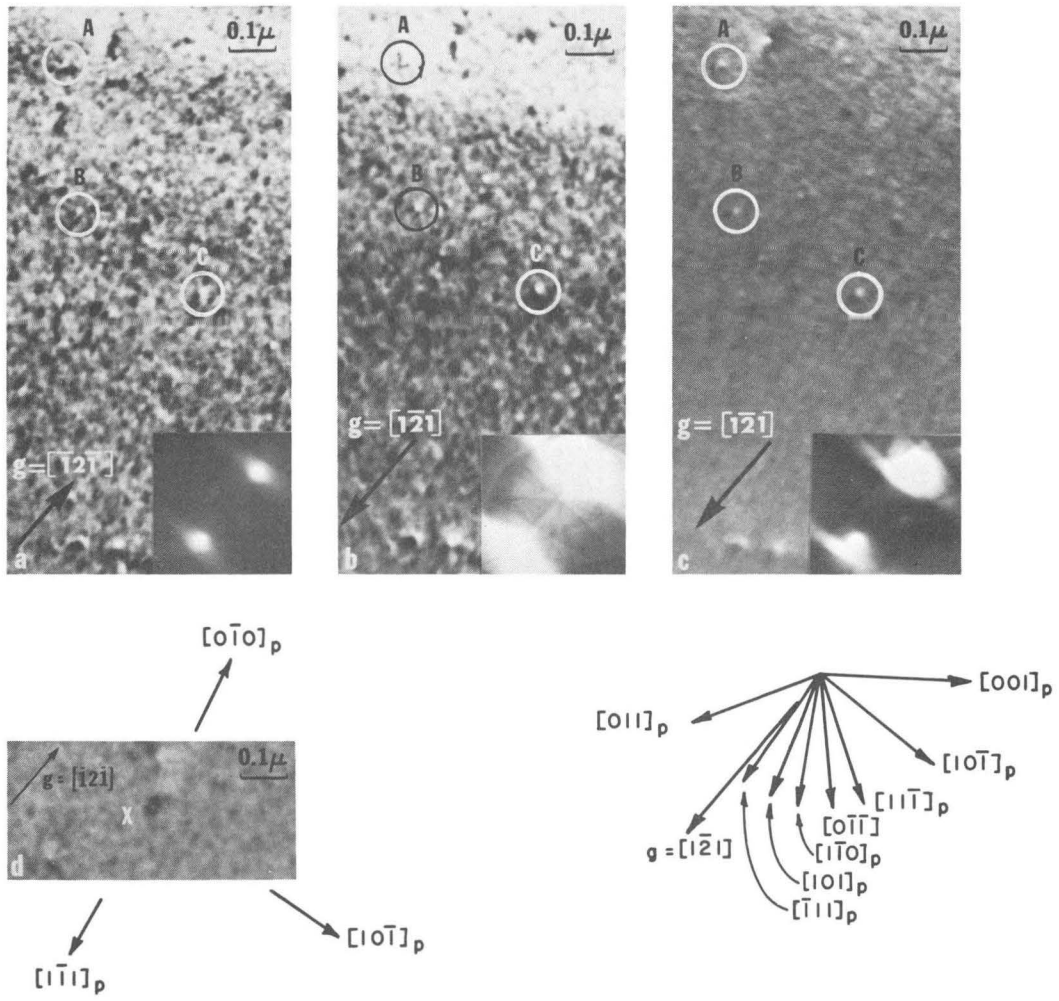
ZN-5934

Fig. 2



ZN-5926

Fig. 3



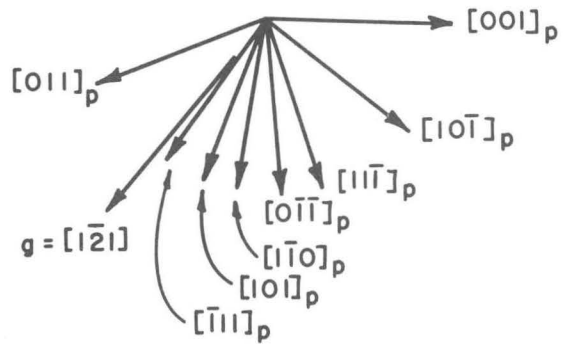
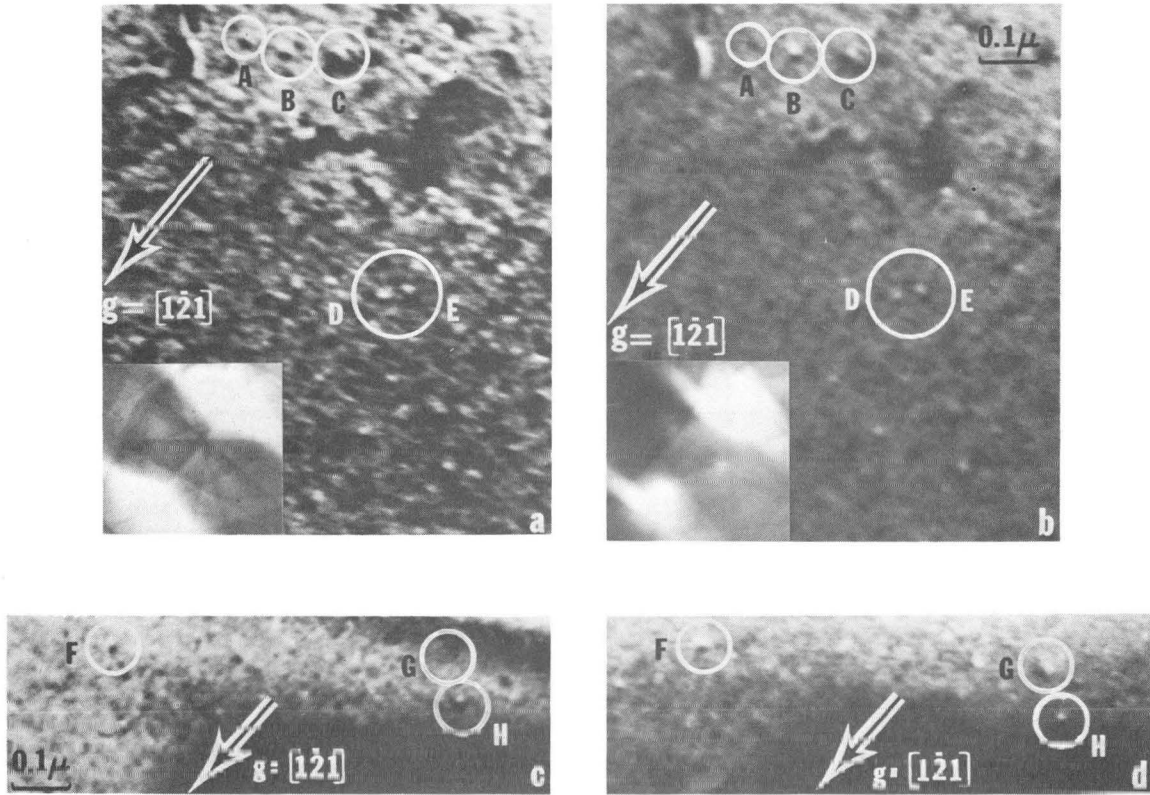
ZN-5927

Fig. 4

Opposing Figure 4

Defect	Bright Field	Dark Field $s < 0$	Dark Field $s > 0$	Burgers Vector	Loop Plane	Approximate Position in Foil
A	Barely visible	Invisible	Visible	$\langle 111 \rangle$	$\{110\}$	Bottom
B	Barely visible	Barely visible	Visible	$\langle 111 \rangle$	$\{110\}$	Bottom
C	Barely visible	Clearly visible	Visible	$\langle 111 \rangle$	$\{110\}$	Top

Foil Orientation: Between $[111]$ and $[012]$ - 14° from $[111]$



ZN-5925

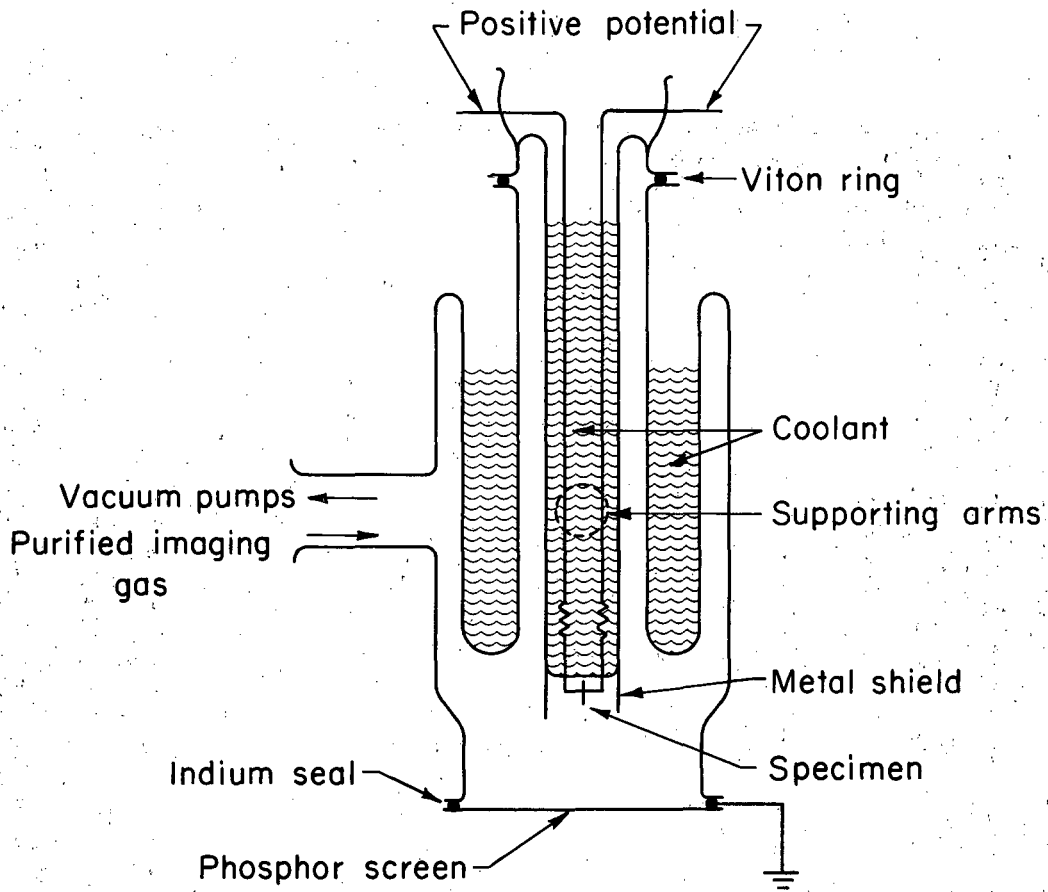
Fig. 5

Opposing Figure 5

Defect	Dark Field $s < 0$	Dark Field $s > 0$	Burgers Vector	Loop Plane	Approximate Position in Foil
A	Clearly visible	Invisible	$\langle 111 \rangle$	$\{110\}$	Top
B	Visible	Visible	$\langle 111 \rangle$	$\{110\}$	Middle
C	Visible	Visible	$\langle 111 \rangle$	$\{110\}$	Middle
D	Barely visible	Visible	$\langle 111 \rangle$	$\{110\}$	Bottom
E	Barely visible	Visible	$\langle 111 \rangle$	$\{110\}$	Bottom
F	Visible	Clearly visible	$\langle 111 \rangle$	$\{110\}$	Bottom
G	Invisible	Visible	$\langle 111 \rangle$	$\{110\}$	Bottom
H	Visible	Visible	$\langle 111 \rangle$	$\{110\}$	Middle

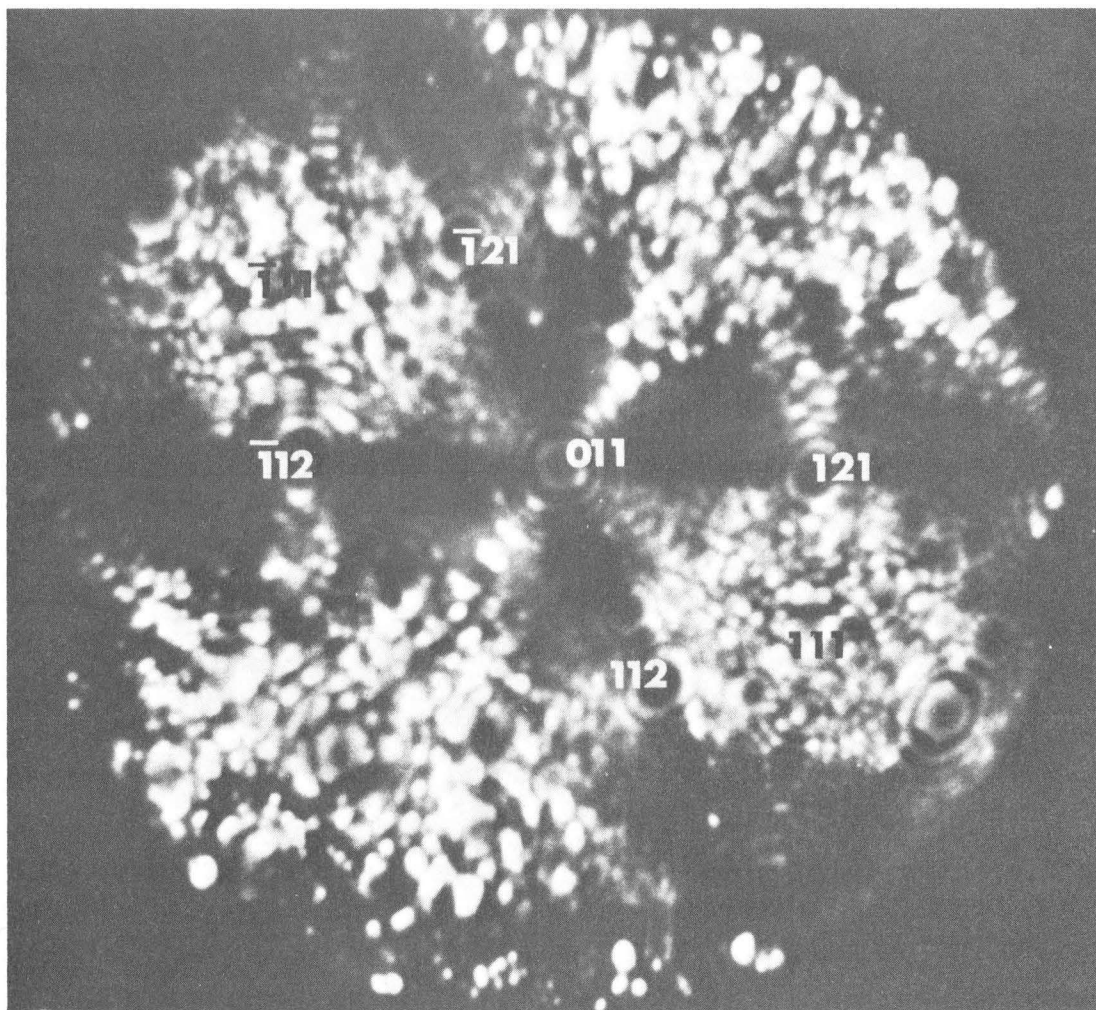
Foil Orientation: Between $[111]$ and $[012]$ - 14° from $[111]$

58a



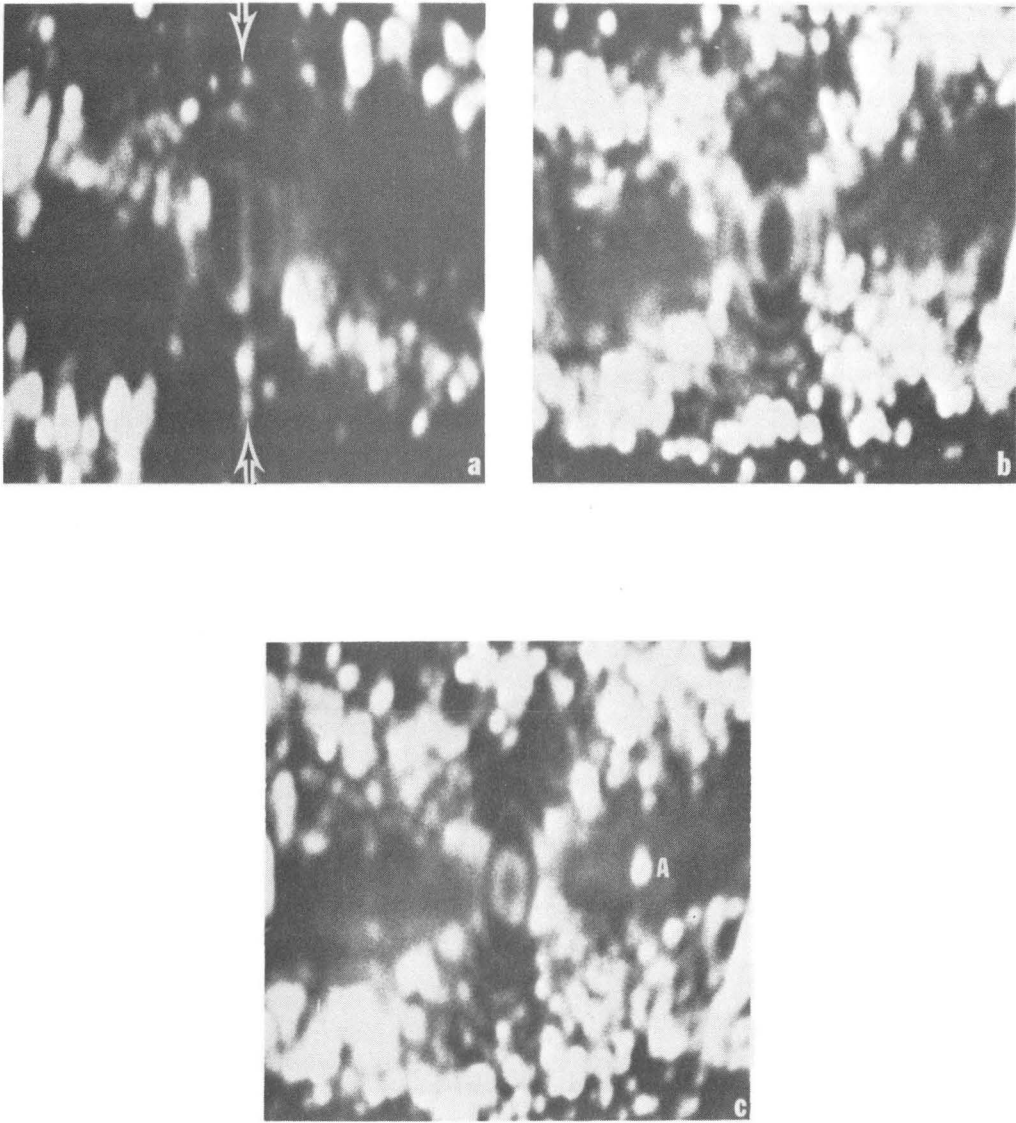
MUB 12515

Fig. 6a



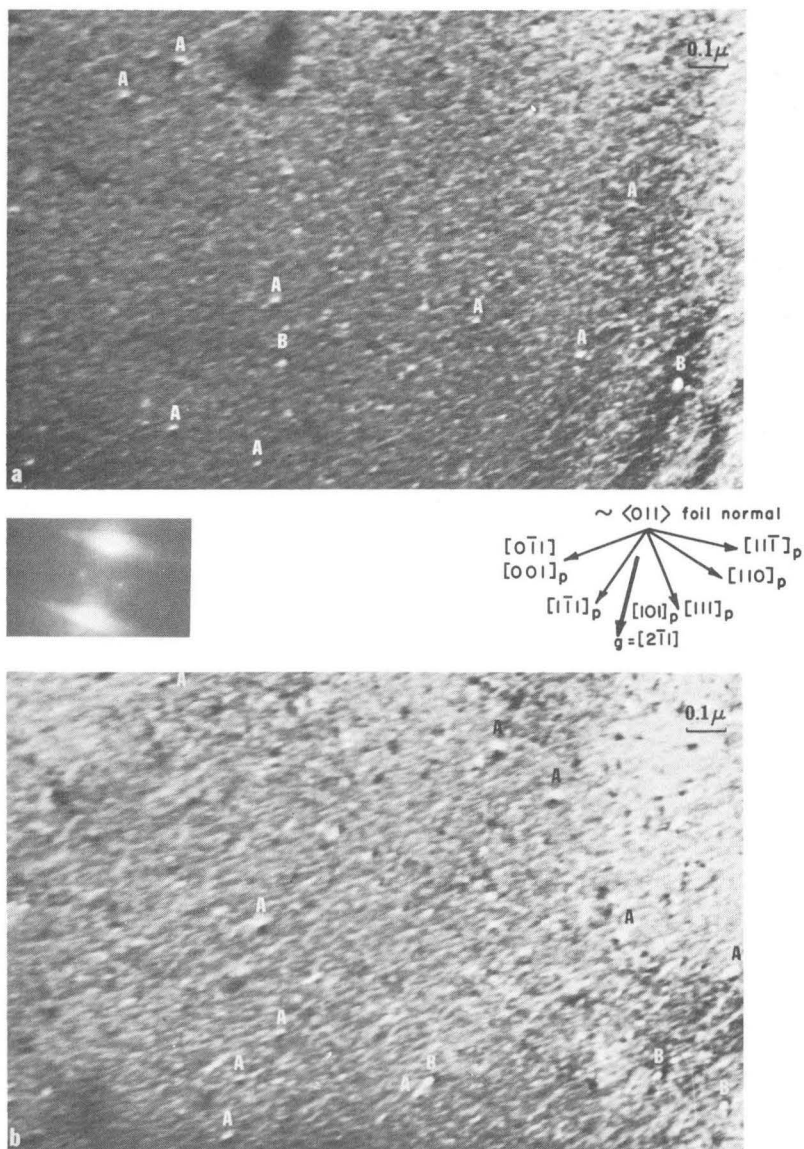
ZN-5924

Fig. 6b



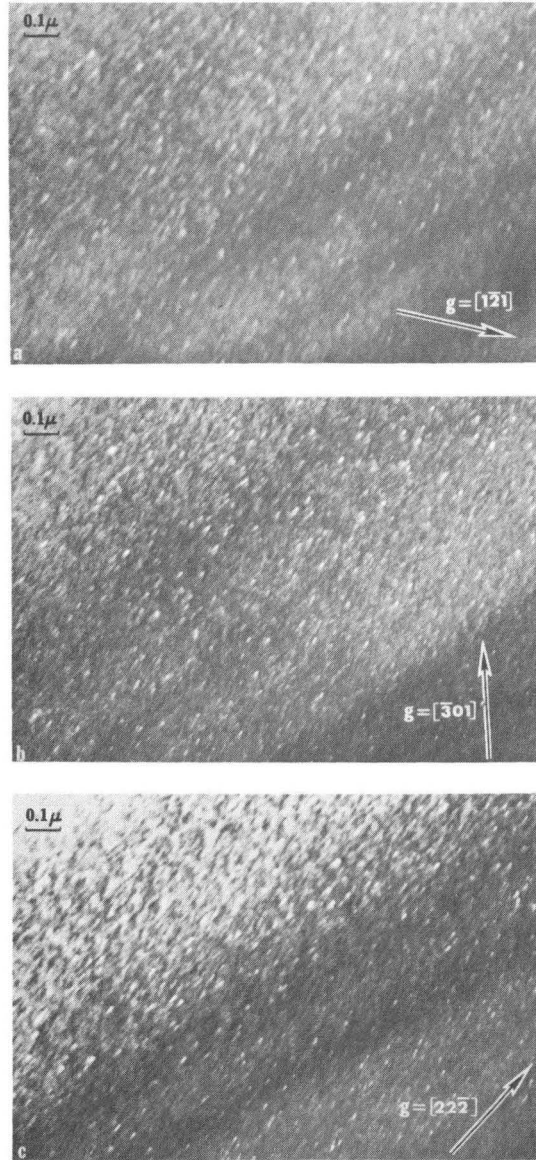
ZN-5933

Fig. 7



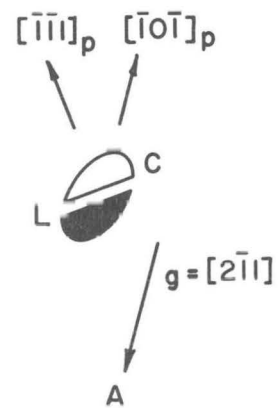
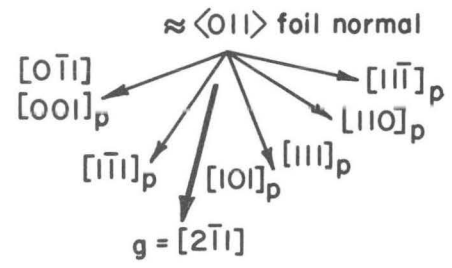
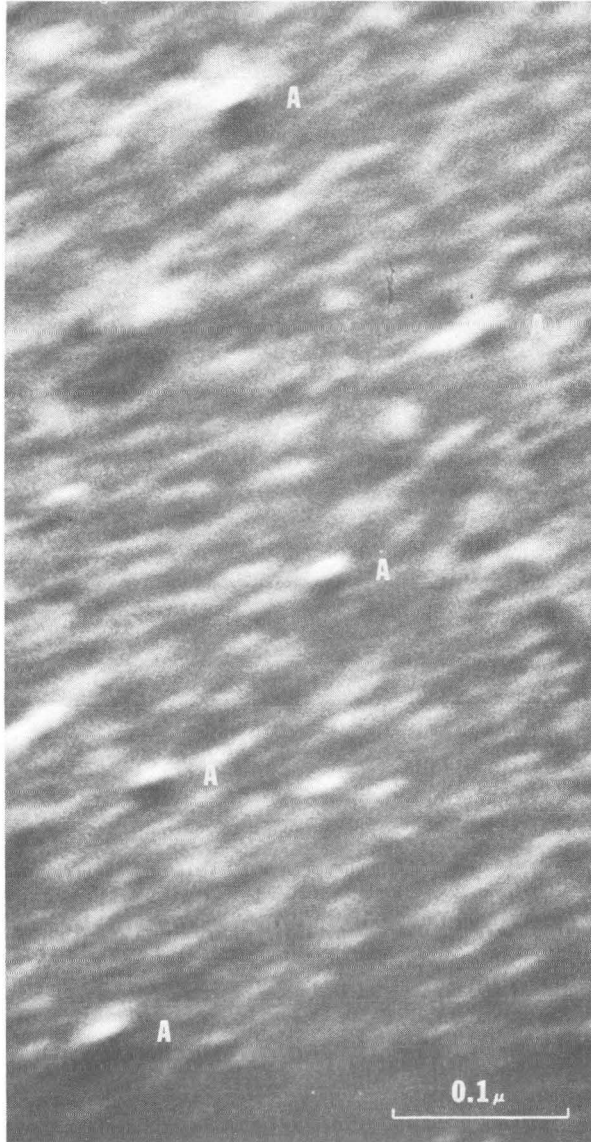
ZN-5923

Fig. 8



ZN-5932

Fig. 9



ZN-5928

Fig. 10

This report was prepared as an account of Government sponsored work. Neither the United States, nor the Commission, nor any person acting on behalf of the Commission:

- A. Makes any warranty or representation, expressed or implied, with respect to the accuracy, completeness, or usefulness of the information contained in this report, or that the use of any information, apparatus, method, or process disclosed in this report may not infringe privately owned rights; or
- B. Assumes any liabilities with respect to the use of, or for damages resulting from the use of any information, apparatus, method, or process disclosed in this report.

As used in the above, "person acting on behalf of the Commission" includes any employee or contractor of the Commission, or employee of such contractor, to the extent that such employee or contractor of the Commission, or employee of such contractor prepares, disseminates, or provides access to, any information pursuant to his employment or contract with the Commission, or his employment with such contractor.

